On-chip light sheet illumination for nanoparticle tracking in microfluidic channels

Théo Travers, Gaétan Delhaye, Martinus H. V. Werts, Denis Gindre, Matthieu Loumaigne

Author version. Accepted manuscript published as *Analytical Methods* **2024**, *16*, 2229–2240

DOI:10.1039/D3AY02290K

On-chip light sheet illumination for nanoparticle tracking in microfluidic channels†

Théo Travers[a], Gaétan Delhaye[a], Martinus H. V. Werts [b], Denis Gindre[a] and Matthieu Loumaigne[a⋆]

A simple and inexpensive method is presented to efficiently integrate light sheet illumination in a microfluidic chip for dark-field microscopic tracking and sizing of nanoparticles. The basic idea is to insert an optical fiber inside a polydimethylsiloxane (PDMS) elastomer microfluidic chip and use it as a cylindrical lens. The optical fiber is in this case no longer seen as only an optical waveguide but as a ready-made micro-optical component that is inexpensive and easy to source. Upon insertion, the optical fiber stretches the PDMS microchannel walls, which has two effects. The first effect is to tone down the intrinsic ripples in the PDMS that would otherwise create inhomogeneities in the light sheet illumination. The second effect is to remove any obliqueness of the channel wall and constrain it to be strictly perpendicular to the propagation of the illumination, avoiding the formation of a prismatic diopter. Through calculations, numerical simulations and measurements, we show that the optimal configuration consists in creating a slowly converging light sheet so that its axial thickness is almost uniform along the tracked area. The corresponding thickness was estimated at $12\,\mu$m, or 10 times the depth of field of the optical system. This leads to an at least six-fold increase in the signal-to-noise ratio compared to the case without the cylindrical lens. This original light-sheet configuration is used to track and size spherical gold nanoparticles with diameters of $80\,$nm and $50\,$nm.

[a] *Laboratoire MOLTECH-Anjou, UMR CNRS 6200, Univ Angers, SFR MATRIX, 2 Bd Lavoisier, 49000 Angers, France*
[b] *Univ Rennes, CNRS, SATIE – UMR8029, F-35000 Rennes, France*
⋆ *matthieu.loumaigne@univ-angers.fr*
† Electronic Supplementary Information available. DOI:10.1039/D3AY02290K

1 Introduction

As stated by Jean Perrin in the 1900s, "Brownian motion is the link between microscopic and macroscopic world".[1] Thanks to Brownian fluctuations, nanoparticles (NPs) and their fluid surroundings can be characterized while at equilibrium. This concept is at the heart of well-established optical and spectroscopic techniques such as dynamic light scattering (DLS)[2] and fluorescence correlation spectroscopy (FCS),[3] and more recent digital microscopic techniques such as differential dynamic microscopy (DDM).[4] Another optical microscopic technique for nanoparticle analysis based on Brownian motion is nanoparticle tracking analysis (NTA) where a number of NPs are imaged at different times in order to reconstruct their Brownian trajectory.[5] This method is used as a tool in cell biology to investigate living-cell mechanisms and behaviors[6]. The main advantage of this technique compared to other Brownian-based methods is arguably the fact that it produces images where FCS and DLS produce curves. Studying images permits one to better picture of the interaction between the particle and their surroundings and more generally to get a better understanding of the overall situation.

NTA requires nanoparticles to be identified against a background and then tracked. The detection limit is set by the signal-to-noise ratio (SNR). The main source of noise is the light emitted by the out-of-focus particles. Indeed, unlike the case of confocal microscopy, every plane of the sample that emits light, even those that are out of focus, will add to the image background projected onto the image sensor. While the light emitted by the particle in focus constitutes the signal, the one emitted by out of focus particle is noise. Consequently, the best strategy for NTA is to only illuminate those zones where the particles are in focus with the image plane. The second source of noise comes from the light used for excitation of the particle but that is ultimately collected by the imaging system. While this light can easily be filtered in fluorescence measurements due to the Stokes shift of fluorescence emission, the situation is more difficult for elastically scattered light. Additionally, the scattered intensity of small particles (i.e. dipolar scatterers) is proportional to the squared volume of the particle and plummets extremely fast (d^{-6}) with the particle diameter d emphasizing the need for excellent rejection of background noise for their detection.

NTA being a sizing technique for NPs in fluids, it is a logical development to combine it with microfluidics in order to manipulate and prepare upstream the fluids before measuring the size of the particles. Hence, traditional dark-field illumination with specialized microscope condensers has already been demonstrated.[7] However, dark field condensers with large numerical aperture must work very close to the sample (a few hundred microns), which makes their use impossible with microfluidic chips whose typical thickness is a fraction of a centimeter.

An alternative lighting setup consists in bringing the excitation light at 90° from the microfluidics channels which is the basic principle of the "ultramicroscope" developed in 1903 by Zsigmondy.[8,9] Excitation light can be brought inside the microfluidics device at 90° for instance from an external microscope objective,[10] an optical fiber guided inside a channel[11] or more simply from external LEDs.[12] Rejection of the excitation light is enhanced due to the total internal reflection happening at the boundary between the coverslip holding the microfluidic device and the air.

In conjunction with optical fiber lighting, 2D micro-optics such as 2D lens[13] or 2D parabolic mirror[14] can be directly microfabricated and embedded with the microfluidics device. However, these 2D optics only focus the light in a plane perpendicular to the optical axis of the collecting objective microscope. Consequently, these 2D optics do not limit the excited area on the optical axis and do not increase the SNR unless the optical setup departs from its classical implementation and the objective is also tilted at 90°[15] or, similarly, using a tilted optofluidic chip.[16] Alternatively, instead of limiting the excitation light beam size, it is possible to reduce the size of the sample by decreasing the vertical size of the microfluidics channel such that it matches the depth of field of the imaging system.[17] Embedded 2D optics that focus the incoming light vertically have also been demonstrated for instance a liquid-filled cylindrical lens[18] or integrated waveguide.[19].

In optical microscopic techniques such as OPFOS (orthogonal plane fluorescence optical sectioning)[20], SPIM (selective plane illumination microscopy),[21] a thin 'sheet' of excitation light is created in the observation volume using modified microscope optics, adding an additional microscope objective. These techniques were adapted for use with microfluidic devices.[22] Such 'light sheet' techniques have seen wide-spread application in 3D imaging of biological samples, leveraging their capability for optical sectioning along the optical axis by dynamically scanning the axial position of the light sheet.

The approach we present here does not target volumetric imaging and employs a static light sheet to achieve highly effective dark field illumination over a thin layer at the center of a microfluidic channel. The light sheet is fully integrated as micro-optics inside the microfluidic chip. The resulting device is compatible with standard inverted microscopes. In contrast to the aforementioned 3D light sheet imaging methods, our method does not require any modified microscope optics. It is inexpensive and easily implemented, creating a static light sheet illumination in a microfluidic channel for the dark-field microscopic tracking and sizing of NPs. The excitation light is brought into the microfluidics chip via an optical fiber and a second optical fiber is inserted inside the microfluidic device perpendicularly to the first one (Figure 1). This second fiber acts as a cylindrical lens for the light exiting the first fiber. The idea is thus to repurpose an optical fiber as a ready-made and inexpensive cylindrical microlens.

First, the optofluidic set-up is presented in which the static light sheet is created. Then, the expected performance of this set-up is calculated with the aid of the ray transfer matrix formalism. Subsequently, the axial width of the light sheet is characterized experimentally. Compared to on-chip fiber illumination without cylindrical microlens, the axial size of the illuminated area inside the microfluidic channel is strongly reduced in the on-chip light sheet configuration, leading to a corresponding increase in signal-to-noise ratio. Finally, as a demonstration experiment, the light sheet is used in the dark-field microscopic tracking and NTA sizing

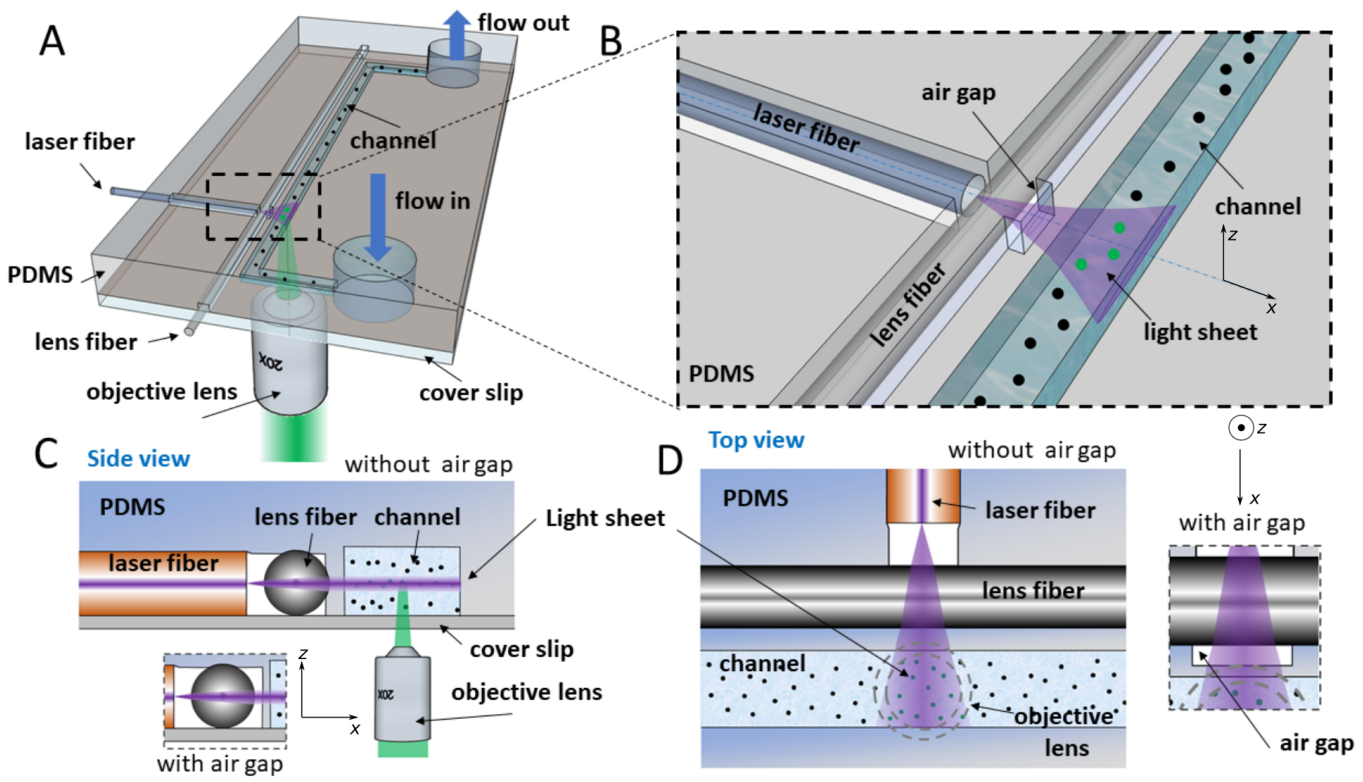

Figure 1 General set-up of the experiment: A) Overview of the microfluidic chip with all the components. B) A 3D view over the area of the light sheet. C) Side view of the positions between the laser fiber, lens fiber, and the fluidic channel. D) View from above, corresponding to the images taken with the microscope.

of gold nanoparticles (GNPs) in water.

2 Material and methods

2.1 Microfluidic chip design

The architecture and optical quality of the microfluidic chip are critical in optofluidics. This is even more true in the present case, since we are dealing with micro-optics and micrometric material irregularities can lead to optical artifacts. The main point of this paper is to prove that an optical fiber can be readily used as a cylindrical lens in order to create a light sheet inside a microfluidic channel. Three geometries are studied and compared (Figure 2). The first geometry (Fig. 2A) acts as a control experiment where the light exiting an optical fiber is directed onto the side of a microfluidic channel without cylindrical microlens. Consequently, the corresponding beam is a divergent cone with an angle determined by the numerical aperture of the fiber. The distance between the non-fluidic channel guiding the optical fiber and the microfluidic channel is around 200 μm in order to guarantee the fluidic sealing of the system.

The second geometry (Fig. 2B) adds an additional non-fluidic microchannel perpendicular to the optical fiber channel into which the second optical fiber is inserted that will act as a cylindrical lens. In this particular configuration, the receiving half of the cylindrical lens is surrounded by air, while the other half, from which the light exits, is surrounded by PDMS. It is assumed that, upon insertion, the optical fiber deforms the PDMS and forces it to partially follow its cylindrical profile. The third geometry (Fig. 2C) adds a notch after the cylindrical lens in order to ensure that both halves of the cylindrical lens are surrounded by the air.

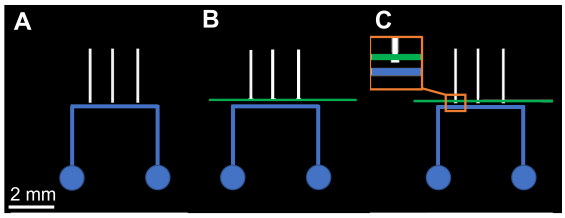

Figure 2 Microchannel architectures used in this study. Blue line: fluidic channel; green line : non-fluidic channel used as a guide for inserting an optical fiber acting as a cylindrical lens; white lines: non-fluidic channel guiding an optical fiber injected with a 405 nm laser. A) Without a lens for focusing the light. B) With a cylindrical lens in contact with the PDMS on its rear side. C) Same as B but with a notch on the rear side of the cylindrical lens to ensure that the lens is surrounded by the air (cf zoom in the orange box). The non-fluidic channel for fiber insertion are designed to have a width of 140 μm and the fluidic channel with a width of 175 μm and a height of 90 μm

2.2 Microfabrication

The microfabrication of chips is achieved by a versatile and fast method using an LCD stereolithography 3D printer.[23] Briefly, a programmable UV LCD screen illuminates a dry-film[24] (Ordyl FP450) with the desired architecture. The chips are designed with

a bitmap file editor with a pixel size corresponding to 31 μm on the LCD screen. The size or number of molds is only limited by the dimensions of the screen (12×7 cm^2) which allows a large versatility in the process. After 10 to 15 minutes of exposure, the insolated dry film is developed in an aqueous K_2CO_3 bath (1% in mass) removing the non-illuminated regions. The final mold is obtained after cleaning the substrate with water. In order to create the microchips, a negative print of the mold is achieved with PDMS (SYLGARD™ 184 Silicone Elastomer). A mixture of the polymer with its curing agent (10:1 by mass) is poured onto the mold and left to cure for 10h at 60 °C. The PDMS chips are plasma-bonded to a glass substrate with the aid of a corona treater.[25]

As for all microfluidics chips embedding an optical fiber, the height of the channel has to accommodate the 125 μm diameter of the optical fiber. This is achieved here by superposing two layers of the dry-film resist. The microchannel height was measured with a profilometer to be at around 90 μm. This is slightly smaller than the fiber that will be inserted and as a consequence, the channel will slightly deform in a useful manner when the fiber is inserted, mitigating two types of imperfections of the current fabrication process. Without a well-collimated beam for the photolithography step, the channels' sides are somewhat oblique and the general shape of the channels is trapezoidal. The corresponding angle can be visualized and roughly estimated by taking an image of the edge of a channel (see Section SI-9). Additionally, as shown previously,[23] the pixel geometry of the LCD matrix used in the lithographic projection can lead to small ripples on the channel surface.

2.3 Optical setup

The optical setup has two parts. The first part, based on micro-optics, creates a light sheet inside a microfluidic channel for particle tracking. The second part, more traditional, is collecting the light scattered from the nanoparticles using a standard microscope objective and projecting it on a camera image sensor.

The micro-optic light sheet part of the setup is schematized in Fig. 1. The excitation source is a 50 mW 405 nm semi-conductor laser (Sony SLD3232VF) driven by a constant-current driver based on a LM317 regulator (See Section SI–1). The laser light is injected into a single-mode optical fiber (Thorlabs S405-XP) with a mode field diameter of around 3.3 μm and a numerical aperture of 0.12. The fiber is 2 m long to allow all non-coupled cladding modes to vanish. In order to have a clean core section, the faces of the optical fiber are cleaved with an optical fiber cleaver (Thorlabs FC-6S). Polishing the fiber was not found to substantially improve the quality of the light-sheet and consequently was not systematically performed. The output power was estimated with a photodiode (Thorlabs DET 025 AFC/M) at around 500 μW. Multimode fibers were also tested but led to a non-uniform illumination due to the speckle emanating from the interferences of the different guided modes.

The optical fiber playing the role of the cylindrical lens (FG105UCA, Thorlabs) is a step-index optical fiber with a 105 μm core and a 125 μm cladding and was used as is after removing its protective acrylate coating with acetone (Its insertion in the microdevices and its optical alignment is explained in section SI–2).

The image collection part of the optical setup is based on a modified Olympus IX71 microscope. The objective used is a 20X, NA 0.75 (UPLSAPO20X, Olympus Corp., Japan), and the image was formed on an industrial CMOS camera (IDS I-3240ML-NIR-GL) operating in global shutter mode. The IDS μEye software provided by the manufacturer is used to capture the video of the Brownian motion. To create z-stacks of the light sheet, a motorized translation stage is used (MKS instruments-New port, MFA-CC) and controlled by a LabVIEW (National Instruments) interface.

2.4 Calculation of the geometric optical parameters of the light sheet

The optical fiber acting as a cylindrical lens has a diameter of 125 μm. It is not a simple monolithic rod of glass, but, like all optical fibers used for guiding light, presents a step (or gradient) in refractive index. The refractive index contrast, defined as $(n_{\text{core}} - n_{\text{cladding}})/(2n_{\text{core}}^2)$, is here very low (≈ 0.004) (the case of gradient index fiber is studied in section SI–3). Thus, the change of index between the core and the cladding does not significantly affect the optical performance of the cylindrical lens.

The elastomeric microchannel acts as a mechanical guide and guarantees that the optical fiber and the cylindrical lens share the same optical plane. In practice, slight misalignments between the cores of the optical fibers can appear due to imperfections in the manufacturing of the optical fiber namely tolerance on cladding diameter (here 125 μm $\pm$ 1 μm), and core-clad concentricity (here $\leq$ 750 nm). Moreover, the optical fiber that brings the light has a low numerical aperture (0.12) and is sufficiently close to the cylindrical lens that the paraxial approximation is valid.

As stated in Section 2.1, two configurations involving the cylindrical fiber microlens were examined. In one configuration (see Fig. 2C), the cylindrical lens is surrounded by an air gap, created by including a lateral notch in the microchannel guiding the fiber. In the paraxial approximation, the effective focal length f_{cyl} (i.e. the distance between the center of the fiber and the position of the focal point) can be calculated as follows[26]:

$$f_{cyl} = \frac{nR}{2(n-1)} \tag{1}$$

with $n \approx 1.47$, the refractive index of the lens fiber for a wavelength in air of 405 nm and R its radius. Here, $f_{cyl} \approx 100\,\mu$m, so that, in order to get a collimated beam, the laser fiber has to be positioned at around 35 μm from the boundaries of the cylindrical lens with a precision of a few micrometers.

In the other configuration (Fig. 2B), the lens fiber has its entry side in air while its exit side is in contact with the PDMS. This case is not traditionally found in textbooks. The ray transfer ('*ABCD*') matrix formalism (Section SI–4) yields a focal distance f_{image} and an object focal distance f_{object}, resp.

$$f_{\text{image}} = \frac{-nR}{n - 2n_{\text{p}} + nn_{\text{p}}} \quad \text{and} \quad f_{\text{object}} = \frac{n\,n_{\text{p}}\,R}{n - 2n_{\text{p}} + nn_{\text{p}}} \tag{2}$$

where n_p is the refractive index of PDMS taken here as 1.447[27]. This leads to an increase of the focal distances compared to the first case with here an object focal distance of $f_{\text{object}} \approx 190\,\mu$m and an image focal distance $f_{\text{image}} \approx 130\,\mu$m. Hence, the accuracy of the positioning of the laser fiber is slightly less critical than with the cylindrical lens surrounded by the air.

Still using the paraxial approximation, Figure 3 shows the waist size w_f of the focalized beam inside the microfluidic channel and the corresponding Rayleigh length z_r as the function of the position s_1 of the laser fiber from the boundary of the cylindrical lens (see Section SI–5 and SI–6 for the corresponding ray transfer matrix calculations). The thickness of the light sheet can be estimated with $2w_f$ while its size along the optical axis can be estimated with $2z_r$ (see Section SI–7 and SI–8).

2.5 Wave-optical numerical simulation of light sheet beam propagation

Numerical simulations of the propagation of the Gaussian beam exiting the optical fiber through the cylindrical lens and then the microfluidics channel were performed using the Wave Propagation Method (WPM) algorithm,[28] as implemented in the Python computer code library 'diffractio'.[29]

2.6 Optimal light sheet depth for particle tracking

Whereas, for most imaging applications, having the thinnest possible light sheet is desired in order to achieve the highest axial resolution, this is not the case for particle tracking. Indeed, a very thin light sheet would lead to particles leaving the observation volume too early and would end prematurely the tracking of the Brownian tracks of the particles. Short tracks lead to great uncertainty in the estimation of the particle size.

The depth of field (DOF), is defined as the distance between two planes where a particle is considered to be in focus. In the ideal case, particles that are illuminated by the light sheet have for image an Airy disk. The further the particle is away from the focal plane, the wider the energy is spread out over a larger Airy disk. Beyond a threshold value, which is a function of the sensitivity of the optical detection system, the particle is not detectable anymore and its scattering signal is buried in the noise. The exact definition of the DOF is context-dependent. In microscopy, where out-of-focus may be described as blur, Berek's formula is often employed for evaluating DOF[30].

$$\text{DOF} = \frac{n\lambda}{(\text{NA})^2} + \frac{ne}{(\text{NA})\,M} \tag{3}$$

which is a sum of two terms, the first one linked to diffraction (Rayleigh criteria) and the other one related to geometrical optics (the circle of confusion), where λ is the wavelength, NA is the numerical aperture and n refractive index of the medium between the coverslip and the objective front lens element, M the magnification, and e is the unit distance of detector elements. Here, this would lead to a DOF of around $1\,\mu$m. However, in the practical context of NTA, particles slightly out of focus can still be tracked and Berek's formula underestimates the effective 'particle-tracking' DOF. Therefore, we use in this work a more pragmatic definition of the depth of field and define it as the maximal distance where the particle can be distinguished from the background noise, and is still trackable. Numerical calculations based on vectorial diffraction of the Point Spread Function (PSF) of the microscope along the axial direction[31] were used to search for the position at which the peak intensity of the particle image reaches a lower limiting value $I_{\text{DOFmin}} = I_b + \sigma_s$ (see Section SI–9). With the optical setup described in Section 2.3 (NA=0.75 and $\lambda = 405\,$nm) the depth of field is estimated around $2.5\,\mu$m. Stated differently, if particles that are $\pm 1.25\,\mu$m away from the focal plane are illuminated by the light sheet, their scattering signal will be so spread out that it will dissolve into the background noise. Based on this consideration alone, the light sheet should have an axial depth of around $2.5\,\mu$m that is to say a waist of around $1.25\,\mu$m at the focal plane.

A light sheet thickness equal to the DOF would initially seem optimal. However, this is not the case in the present set-up applied to nanoparticle tracking in a microfluidic channel. Firstly, a focused beam with a $1.25\,\mu$m waist is not obtainable due to the size of the core of the optical fiber ($\approx 3\,\mu$m) and the limited numerical aperture of the cylindrical lens (Fig. 3). More importantly, this would also mean a Rayleigh length z_r much smaller than the width of the microchannel and consequently a non-even thickness of the light sheet along the microchannel and the detection area. Positioning the optical fiber close to the object focal plane of the cylinder lens and thus obtaining a quasi-collimated beam (instead of a focused one) is an interesting configuration since, as it will be shown, the light sheet is sufficiently thin and almost even thickness on all the field of view of the microscope.

2.7 Optimal image acquisition frame rate

In purely Brownian motion, the characteristic distance traveled by a spherical particle during the period of one frame of the tracking camera can be derived from its mean squared displacement $MSD = \langle(\Delta x)^2\rangle$ [32]:

$$\langle(\Delta x)^2\rangle = 2dDT = \frac{2d\Delta t k_B T}{6\pi\eta(T)r} \tag{4}$$

where $\Delta x = x_{n+1} - x_n$ is the displacement of one particle during one frame period, D is the diffusion coefficient, d the degrees of freedom of the particle, Δt the camera frame period, k_B is the Boltzmann constant (exactly $1.380\,649 \times 10^{-23}\,\text{J K}^{-1}$), T the temperature in K, $\eta(T)$ the dynamic viscosity of the fluid (at the specified temperature) in Pa s and r the hydrodynamic radius of the particle in m.

The hydrodynamic radius (and the hydrodynamic diameter $2r$) define the effective sphere whose diffusion in the liquid is described by the Stokes-Einstein-Sutherland equation, linking the hydrodynamic radius to the experimentally determined diffusion coefficient D. The hydrodynamic diameter represents the physical size of the particle plus a boundary layer accounting for the interactions of the particle with the surrounding liquid medium. Interestingly, the translational Brownian motion of non spherical particles can still be associated with an effective sphere of a given hydrodynamic diameter.

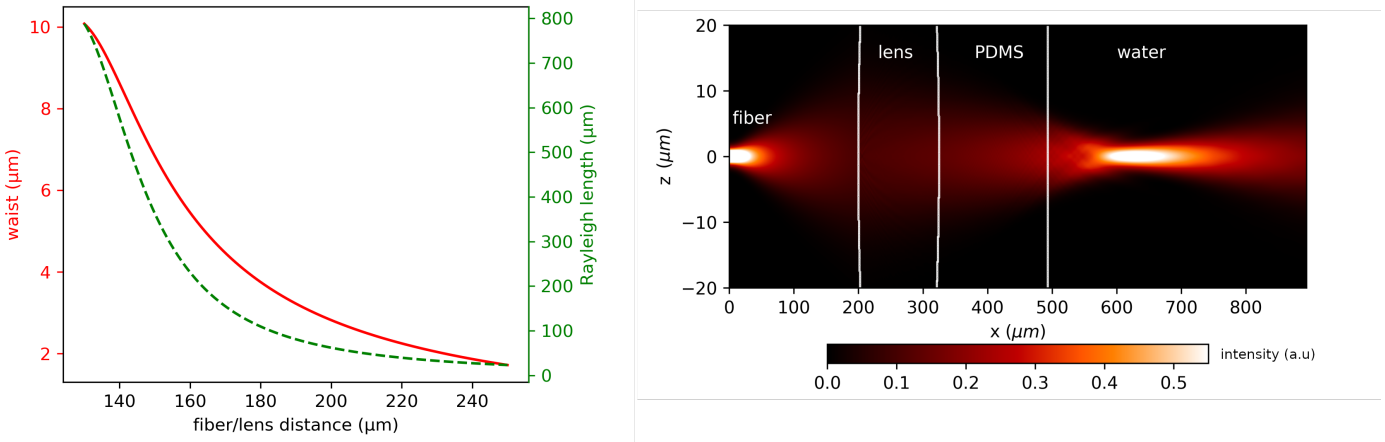

Figure 3 . Left panel: Waist at focal plane w_f and Rayleigh length z_r of the Gaussian beam focussed by the cylindrical lens inside a microfluidic channel filled with water as a function of the position s_1 of the laser fiber from the *boundary* of the cylindrical lens (not its center). The calculation (paraxial approximation) corresponds to the case drawn in Fig. 2B, where the exit side of the cylindrical lens is pressed against the PDMS wall. The waist at focal plane $2w_f$ has to be compared with the depth of focus of the optical system and should ideally have the same size. The Rayleigh length $2z_r$ has to be compared to the field of view of the imaging system or, if it is smaller, to the lateral size of the microfluidic channel. In order to guarantee that the light sheet is homogeneous along the measurement area, $2z_r$ should be close to the size of the field of view. Right: wave-optical numerical simulation of the axial profile (*i.e.* light sheet thickness) with the same optofluidic device configuration and a fiber distance–lens distance of $200\,\mu$m.

For optimal precision in determining the diffusion coefficient (and hydrodynamic diameter) of the particles using NTA, the number of points N in a track must be maximized. The relative error over the estimation of D is following a $\frac{1}{\sqrt{N}}$ behavior.[33] However, the dwell time of the particle inside the observation area is limited by the DOF of the optical setup. Without changing the optical setup and the NA of the objective, the only way to increase the number of points N per track is to increase the framerate of image acquisition. Nonetheless, it can be increased up to a limit where the displacement Δx is smaller than the localization precision[34] of the particle. As a consequence, for a given experiment where the particle size is already known and the optical setup set a DOF, there exists an optimal frame rate.

2.8 Formulation of nanoparticle and fluorescent dye solutions

The 50 nm and 80 nm gold NPs (GNPs) were stabilized in aqueous solution by $2 \times 10^{-4}\,\mathrm{mol\,L^{-1}}$ sodium (±)-α-lipoate in the presence of 1 mM NaOH. The solutions were prepared according to a previously described procedure, starting from commercially available citrate-stabilized GNPs (BBI Solutions or Sigma-Aldrich), replacing the unspecified citrate medium with a solution of sodium lipoate and NaOH, through several centrifugation-concentration-resuspension cycles.[35] The centrifugation steps were 30 min each, at $800 \times g$ and $400 \times g$ centrifugal acceleration (RCF), for 50 nm and 80 nm gold NPs, respectively.[36]

Polystyrene latex beads of 500 nm and 220 nm diameter were used as light scatterers (Fluoresbrite® 24054, Polyscience). The particles have a size dispersion of 3% and 5% respectively. The fluorescence of the particle was negligible compared to their scattering signal at 405 nm. Taking a $n = 1.62$ as the refractive index of polystyrene at 405 nm the scattering cross-section of the 220 nm diameter nanoparticle in water is estimated via Mie theory[37] at $15\,000\,\mathrm{nm}^2$. The stock solution is 3.64×10^{11} particles/mL and we used a 1000-fold dilution.

The uniformity of the light sheet was characterized using an aqueous fluorescent solution of an Atto 390 dye derivative (Atto 390 alkyne, Sigma-Aldrich) at $1 \times 10^{-5}\,\mathrm{mol\,L^{-1}}$ (see Section SI–10).

2.9 Determination of the thickness of the light sheet

The limited axial resolution of a conventional optical microscope would only give a rough estimation of the thickness of the light sheet. Confocal microscopy or deconvolution of a stack of images[38] could be used to determine the thickness with greater precision. As a more direct approach, we adapted the method used by Deschout *et al.*,[19] which is based upon an earlier described technique.[39]

The thickness of the light sheet is probed with the scattering signal of sub-resolution particles (point sources). Each particle is sampling the light beam and reports the local intensity of the light sheet *via* its scattering signal. However, since wide-field microscopy is used, out-of-focus particles are still present in the images. These should not be taken into account. The removal of these out-of-focus particles was achieved here via numerical post-processing.

A z-stack of 200 nm step images is taken across the axial depth of the light sheet. For the numerical post-processing, the same methods as in the ImageJ plugin Trackmate[40] were used for spot detection. First, a LoG (Laplacian of Gaussian) filter is applied to each image with a standard deviation of the Gaussian kernel related to the expected theoretical diameter of the Airy disk. Particles in focus are assigned to local maxima in the filtered image. A contrast value $C = (I_{\mathrm{in}} - I_{\mathrm{out}})/(I_{\mathrm{in}} + I_{\mathrm{out}})$ is computed for each

detected particle where I_{in} is the mean intensity inside the particle area (using as radius its Airy disk diameter divided by 2), and I_{out} is the mean intensity in a ring ranging from its radius to twice its radius. This contrast C is an estimate of how much in focus a detected particle is. The intensity $I(z)$ of the light sheet for a given z axial position is obtained weighted by the contrast C, *i.e.* $I(z) = 1/N(z)\sum_{n=1}^{N}(z)C_n I_{\text{in}}(n)$ where $N(z)$ is the number of detected particle in the slice at position z. Finally, the light sheet thickness is obtained by fitting the full experimental $I(z)$ curve by a Gaussian and assigning its thickness to two times the standard deviation σ, that is to say, the full width at $I_{\max}/e^2$ where $I_{\max}$ is the maximum intensity. The the full width at half maximum (FWHM) is obtained via $FWHM \approx 1.17\sigma$ (see Section SI–8).

2.10 Particle tracking and track analysis

Single particles are detected, tracked, and linked using Trackmate[40] (see Section SI–11). We derive the diffusion coefficient D for each track by studying the mean square deviation (MSD) $\langle(\Delta x_n)^2\rangle$ and the covariance $\langle(\Delta x_n)(\Delta x_{n+1})\rangle$ of the displacements[34,41]. This method corrects the errors induced in the raw MSD by the motion blur caused by the diffusion of the particle during the integration time of one frame and the localization error mentioned before. Special care was also taken in order to take into account the drift of the NPs due to residual flow in the microfluidic channels (see Section SI–12).

2.11 Signal-to-noise ratio

Nanoparticle tracking requires the determination of the position of a particle identified against a noisy background, and its success depends on the signal-to-noise ratio of nanoparticle spots in the image. Here, we determine the signal-to-noise ratio (SNR) from the intensity value of the brightest pixel I_p of a particle spot as the measure of signal. The noise level I_b is taken as the mean value of the light-sheet area after a low-pass filter on the image (median filter, 20 pixels). Thus, the SNR is defined here as :

$$\text{SNR} = \frac{I_p}{I_b} \tag{5}$$

3 Results

3.1 Comparison of three device architectures

Three architectures for on-chip dark-field illumination using an optical fiber (Fig. 2) were studied and compared. Figure 4 collects the three architectures and shows the resulting dark-field images of nanoparticle solutions. For direct comparison of the quality of the dark-field images between geometries, a standardized sample of 220 nm latex beads in water was injected in each case, and the same laser power was used.

Configuration A, in which illumination is achieved by the direct output of the laser fiber, without a cylindrical microlens (Fig.4-A), serves as the benchmark against which the efficacy of other micro-optical configurations is compared. In this configuration, the illuminated volume has a truncated cone shape. The SNR for particle tracking is found to be 2. Using a z-stack pile of images, as explained in Section 2.9, the thickness of the light sheet is measured at approximately 100 μm (see insert of Fig. 6). This value is in good agreement with the one obtained through calculation with the propagation of a Gaussian beam in the paraxial approximation (see Section SI–7). The lateral profile of the divergent illumination cone is presented and discussed in Section SI–10.

Configuration B (Fig. 4-B) introduces a cylindrical lens to focus the light beam emanating from the fiber along the z optical axis, which can not be seen in this xy image, thereby creating a light sheet for illumination. The SNR with the cylindrical lens for the scattering of 220 nm diameter beads is estimated at $SNR = 12$. This represents a 6 times increase of the SNR compared to the case without a cylindrical lens, as the light sheet predominantly illuminates particles within the microscope's depth of field.

Configuration C, akin to B but incorporating an air notch, would in theory provide an even better light sheet by augmenting the refractive index change. Unexpectedly, this configuration C produces a light sheet with two notable imperfections (Fig. 4-C): the emergence of fringe patterns within the light sheet and a tilted light sheet, which results in particles at the field of view's border appearing out of focus. The incorporation of an air notch, rather than augmenting the light-sheet's efficiency, introduces two significant artifacts. These anomalies are due to the imperfections of the PDMS channels at the micrometric scale during their microfabrication.

The first problem is the surface roughness of the PDMS, which is not optically discernable but can distort the light sheet. An irregular surface of the PDMS after the cylindrical lens can create fringes with different intensities in the channel. This effect is a well-known cause of contrast loss in light sheets and dark-field microscopy inside microfluidics devices. Chemical methods to smooth the microchannel surface have been proposed.[42] The influence of the roughness of the PDMS wall is examined semi-quantitatively through numerical simulations in Section SI–14. These simulations show that the fringes are visible for a surface roughness with a standard deviation as low as 500 nm.

The second problem is the non-verticality (obliqueness) of the microchannel sides (see also Section SI–14). These should ideally be vertical. Control on the verticality of the relatively high PDMS channel used here depends on the exposure condition of the photoresist and the etching process.[43]. In Fig. 4-C, the PDMS channels are trapezoidal (oblique walls) and they act as a prism and deflect the light sheet. This situation is schematized in Fig. 5A. As a result, only the beads on a portion of 40 μm of the 200 μm wide microfluidics channel are in focus. From the image in Fig. 4-C2 and the known DOF of the optical setup, the angle of deflection is estimated at 16° which is in good agreement with the expected deflection due to the angle of trapezoidal PDMS microchannels. Additionally, the point spread function (PSF) of the scattering particles is not symmetric anymore.

Compared to configuration C, configuration B features one half of the cylindrical lens encased in PDMS, leading to a disappearance of the prismatic effect of the PDMS channel and a large attenuation of the fringes effect. We attribute these to the reshaping of the PDMS channel by the cylindrical lens. We hypothesize that the microfluidic channel adjusts to the cylindrical shape of the lens (see Fig. 5B), thanks to the elasticity of PDMS. This stretch-

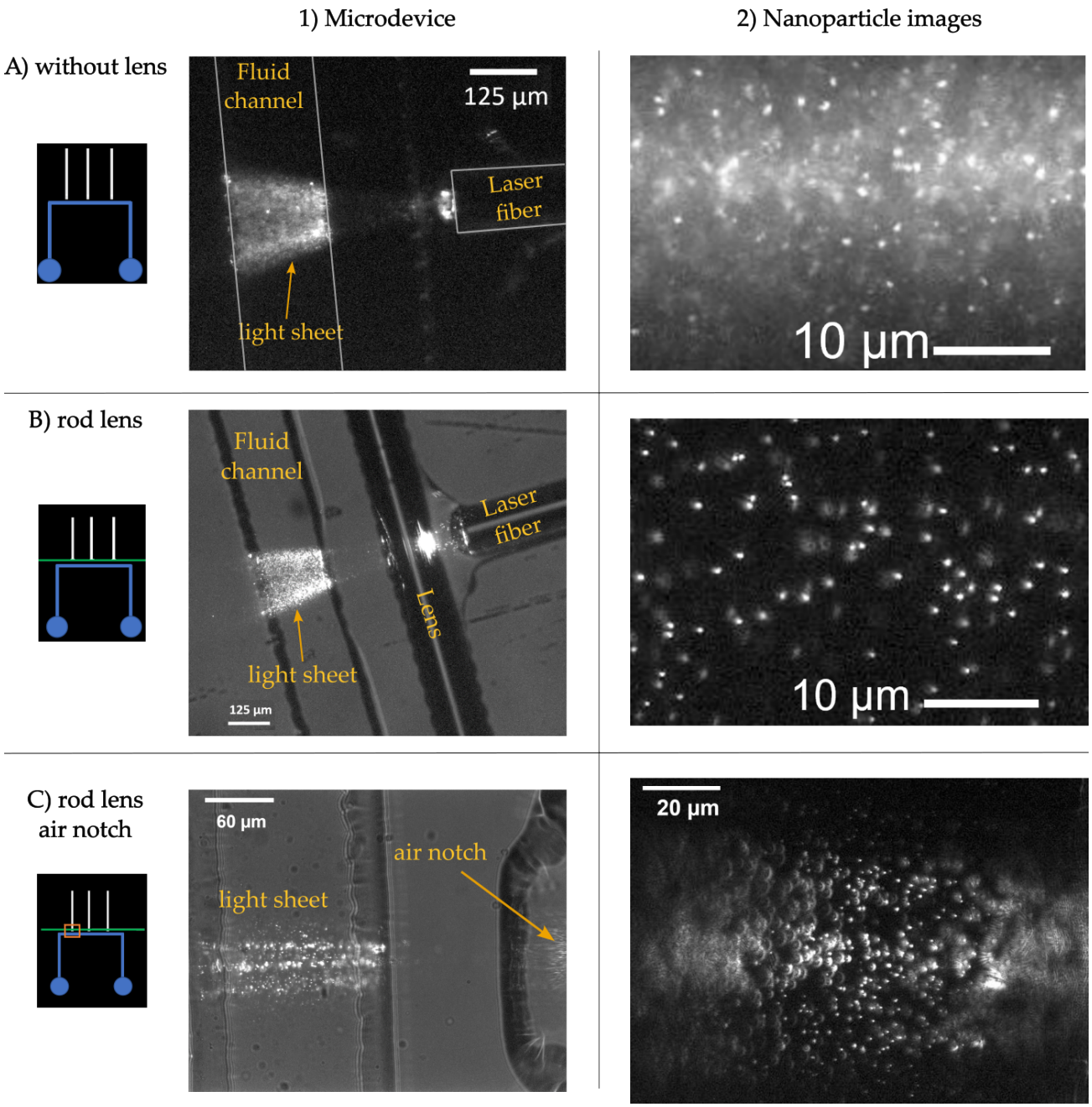

Figure 4 Optical microscopy images of the microdevices (column 1) and corresponding light-sheet visualization (column 2) of 220 nm latex beads in water for each of the three configurations defined in Figure 2. Configuration (A) has fiber illumination of the channel without the cylindrical lens, yielding a signal-to-noise ratio (SNR) of 2. Configuration (B) has the microfluidic device equipped with a cylindrical lens, with an increased SNR of 12. The slight deformation observed in the PDMS channel of this particular device, is an exception and absent in most other instances. Configuration (C) adds an additional air notch between the cylindrical lens and the illuminated fluid channel aimed at further increasing SNR. However, fringe patterns in the light sheet appear together with out-of-focus illuminated zones as a consequence of the light sheet being deflected by the oblique walls of the channel. The fringe patterns are attributed to the irregular surface of the channel.

ing of the PDMS interface tends to attenuate the roughness of the PDMS wall and straightens it from its unwanted initial trapezoidal shape. It is finally configuration B which has the best static light sheet illumination performance, given the limitations on the quality of the moulds and PDMS microchannels posed by the low-cost fabrication process.

3.2 Shape of the optimal light sheet

Optimal light sheet illumination is thus obtained with a cylindrical lens in configuration B (Figure 4B) with a distance of 165($\pm$5) μm between the optical fiber and the front of the lens. In this configuration, the laser beam is slightly convergent. Compared to direct fiber illumination without a cylindrical lens (Fig. 4A), the contrast of the individual particles is greatly improved as a result of the absence of illumination of out-of-focus particles.

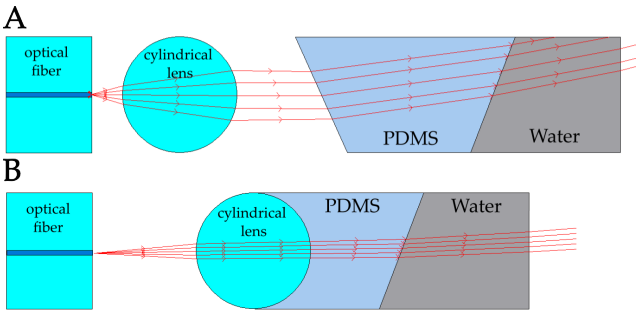

Figure 5 Tentative explanation for the artefacts (fringes and out-of-focus illumination) observed in configuration C and their absence in configuration B. (A) Configuration C with an air gap between the cylindrical lens and the PDMS wall, where the non-ideal trapezoidal shape of the PDMS wall functions as a prismatic diopter, causing vertical deflection of the light sheet. (B) Possible modification of the shape of the PDMS wall by the pressure of the cylindrical lens in configuration B. The introduction of the lens distorts the PDMS, eliminating its prismatic properties. This also attenuates the fringe patterns attributed to the surface roughness of the PDMS, thereby enhancing the uniformity of the light sheet.

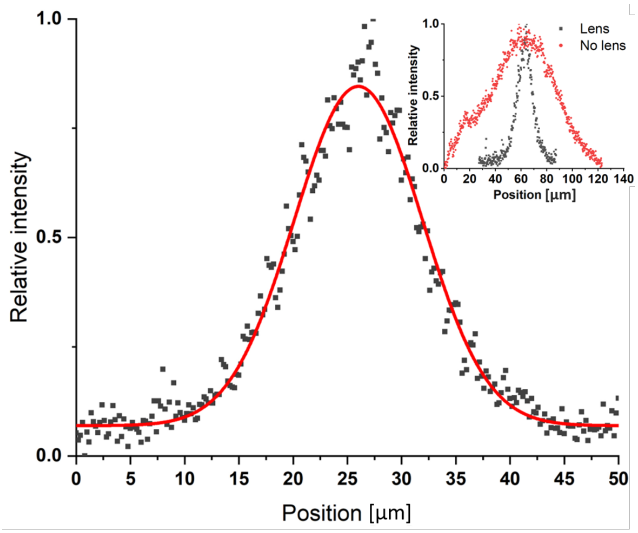

Figure 6 Normalized particle number weighted by their contrast along the light-sheet axial profile for a lens/fiber distance of $165(\pm 5)\ \mu$m and 220 nm diameter beads for the slightly convergent beam configuration. The Gaussian fit gives a waist around $10\,\mu$m and consequently a light-sheet thickness around $20\,\mu$m. The top right corner shows the comparison of the light-sheet profile without a lens in red and with a cylindrical lens in gray.

As Figure 6 shows, the light sheet is very thin compared to the cone-shape illumination directly from the fiber exit without cylindrical lens. The corresponding waist is measured to have a width of approximately $10\,\mu$m. Calculation in the paraxial approximation using the experimental conditions gives a beam diameter ($2w_f$, two times the waist) of $10\,\mu$m inside the microchannel. The discrepancy between the measured light-sheet thickness ($20\,\mu$m) and the predicted value ($10\,\mu$m) can be attributed to two factors. Firstly, there are uncertainties in the measurement technique employed here. Secondly, the measurement is carried out over a region that is on the order of the Rayleigh length, causing the waist w_0 of the light sheet to take values between w_0 and $\sqrt{2}w_0$. This discrepancy inherently leads to an overestimation in the measurement of the waist.

3.3 Application of microfluidic light sheet illumination to nanoparticle tracking analysis

Using the optimal light sheet illumination conditions as described above, we have tracked the Brownian motion of 80 nm and 50 nm spherical gold NPs in dark-field videomicroscopy. Figures 7A and 7B present representative darkfield images of the nanoparticle solutions obtained with the light sheet. The corresponding video sequences can be found in the Electronic Supplementary Information (SI–16). The SNR for the 80 nm and 50 nm diameter GNPs are respectevely around 20 and 10. The latter result is very interesting considering the relatively small scattering section of 50 nm GNP at $\lambda = 405$ nm (namely $\sigma_{\text{scatt 50nm}} = 7600\,\text{nm}^2$ and $\sigma_{\text{scatt 50nm}} = 470\,\text{nm}^2$). The contrast could be further increased, firstly by using a laser at the plasmon resonance of the particle (approximatively a two times increase in the scattered intensity) and by injecting more power inside the optical fiber. Hence, it should definitely be possible to image and track smaller metallic nanoparticles. Images presented here were obtained with a modest laser power of only $500\,\mu$W at the output of the fiber, corresponding to a light flux through the sample of around $15\,\text{W}\,\text{cm}^{-2}$ at the center of the microchannel.

Figures 7A and 7B also present on the right the histograms of the hydrodynamic diameter of the 80 nm and 50 nm GNPs obtained from respectively 3050 and 100 Brownian trajectories measured at 20 °C. The average values for the hydrodynamic diameter are respectively 90 nm and 60 nm which are slightly bigger than the expected physical diameters accounting for the increase of the hydrodynamic radius due to the ligands and electric double layer at the surface of the GNP.[44]

4 Discussion

The calculated and simulated data provided in Figure 3 serve as guides for initial design and optimization. In practice, the gap between the optical fiber and the cylindrical lens is fine-tuned by optimizing the signal-to-noise ratio (SNR) with which the particles are detected. One possibility for increasing SNR would be by strongly focusing the light from the optical fiber onto the center of the fluidic channel, but this approach has several draw-backs. Firstly, such intense focusing leads to a significantly constrained area of study, since strong focussing also entails a strong defocussing before and after the focal point. Secondly, it requires an ultra-thin PDMS layer between the lens and the microfluidic channel, leading to microfluidic leaking. Lastly, spherical aberrations may occur, given that short distance of the optical fiber from the lens causes a deviation from paraxial conditions.

In the case presented here (with particles having scattering cross-sections $\sigma_{scat} > 470\,\text{nm}^2$), the best configuration for observing the particles is to have a slightly converging beam by placing the fiber near the focal plane of the cylindrical lens. This positioning guarantees an adequate light-sheet thickness to detect particles with a high SNR, and an almost homogeneous light-sheet

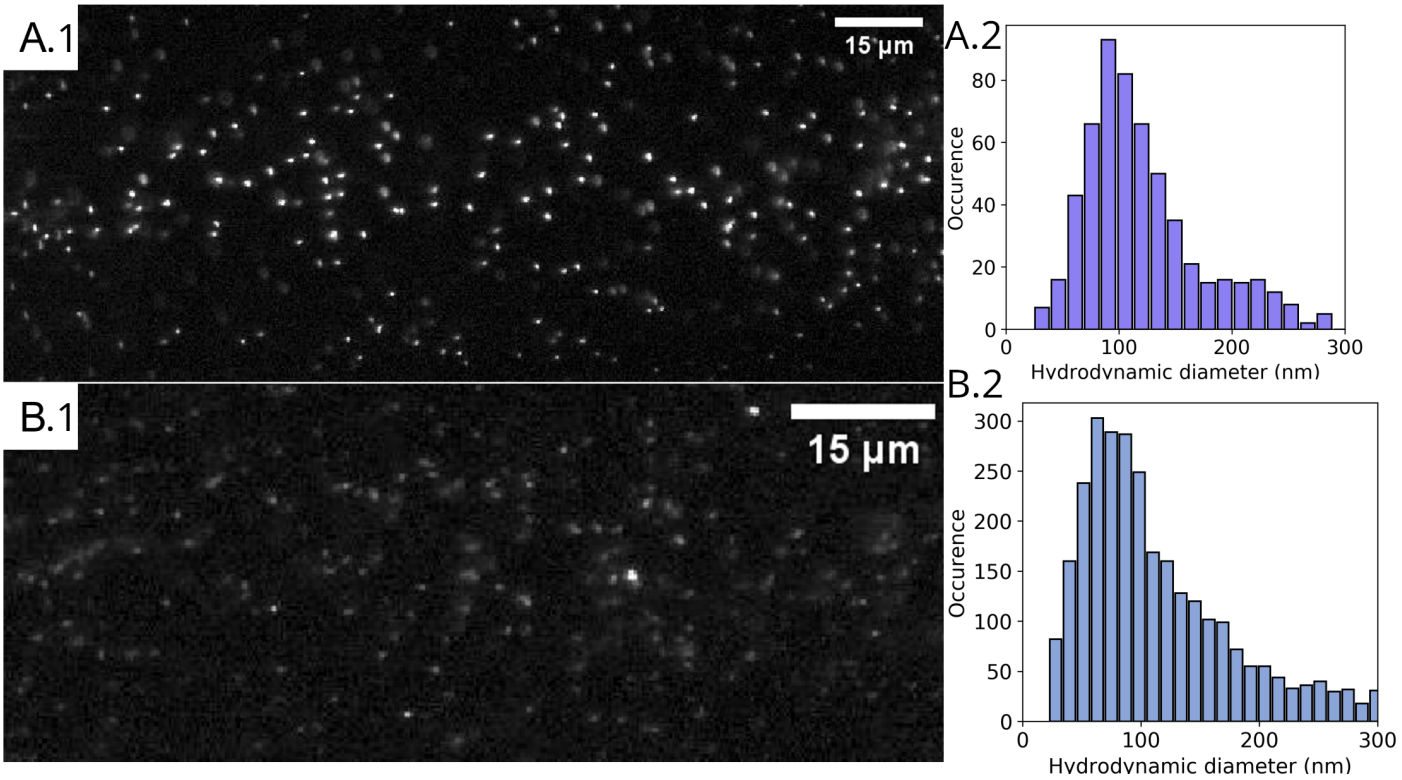

Figure 7 Dark-field images of the scattering of spherical gold nanoparticles and corresponding Histogram of the hydrodynamic diameter obtained by NTA having a diameter of A) 80 nm and B) 50 nm. Exposure time : 6 ms See Section SI–15 for a link to the related movies.

thickness across the study zone.

Exploring beyond this initial demonstration, it is probable that particles with a scattering cross-section much smaller than those analyzed here can be detected. In Figure 7, the background noise primarily comes from the image sensor baseline, with the signal corresponding to the particles having pixels nearing saturation. Thus, by augmenting the laser power injected into the fiber, it will be possible to monitor smaller particles at increased frame rates. Future investigations will aim to identify the minimum optical scattering cross-section required for particle detection. Beyond direct identification of particles in the image, particles could alternatively be detected and characterized by autocorrelation and Fourier methods, such as differential dynamic microscopy (DDM).[4]

An important additional factor for ensuring the quality of the light sheet is avoiding illumination of the microscope slide surface. Nanoparticles commonly adsorb onto this surface, creating a highly diffusive layer. If this layer is illuminated by the light sheet, the signal-to-noise ratio takes a sharp decline due to the stray light from surface scattering. Given the positioning of the fiber core at about 65 μm from the surface, and the light-sheet thickness of approximately 20 μm (as shown in Figure 6), these issues are readily avoided. This positioning also provides the added advantage of preventing the tracking of particles interacting with the surface[45], and only tracking particles undergoing free Brownian motion.

While minor fringe effects as observed even with configuration B do not impede particle tracking, such phenomena could present challenges for more complex analytical tasks. Specifically, identifying particles based on the color of the scattered light under polychromatic illumination may be adversely affected by these stripe effects. This underscores the importance of optimizing the light-sheet homogeneity, especially when employing color-based discrimination techniques to elucidate particle characteristics.

The original method presented in this work for achieving dark field illumination to track nanoparticles has several advantages over other techniques. Unlike fabrication approaches that necessitate access to extensive cleanroom infrastructure and involve complex microfabrication processes, our method requires only a single-step fabrication with a resolution of approximately 40 μm, simplifying the preparation significantly. In comparison with other light sheet microscopic approaches, the optical setup is notably straightforward, eliminating the need for meticulous alignment of condensers or microscope objectives, and working with a standard inverted microscope. The task of inserting and precisely positioning the fiber with an accuracy of 10 μm, which may seem daunting at first, becomes surprisingly manageable with minimal practice. A steady hand and visual feedback under a microscope are sufficient to achieve the required precision. Furthermore, our light sheet operates at a sufficient distance from the surface, thereby minimizing any potential influence from surface interactions. Furthermore, it does not rely on proprietary consumables, contrasting with systems like Nanosight[46]. Ultimately, this technique uses microfluidic channels as mechanical guide and is naturally suited for implementation within microfluidic chips. Measurements of Brownian motion, however, necessitate the ces-

sation of fluid flow within the chip prior to data acquisition. This can be achieved through the use of external valves.[47]

5 Conclusions

In this study, we have successfully demonstrated a straightforward, cost-effective, and efficient method for creating a static light sheet within a microfluidic chip with a design optimized for tracking and sizing nanoparticles. An optical fiber, usually viewed only as an optical waveguide, was repurposed as a cylindrical lens within the chip. One interesting and unexpected effect of inserting the optical fiber in the microfluidic circuit is the stretching of the PDMS walls, leading to reduced inherent ripples at the surface of the PDMS and straightening out a residual oblique angle which otherwise would deviate the light beam.

Through calculations, numerical simulations, and measurements, this study establishes an optimal optical configuration for particle tracking: positioning the guiding fiber exit with respect to the cylindrical lens such that a slowly converging light sheet is formed inside the microfluidic observation zone. This configuration allows for a near-uniform axial thickness along the tracked area, estimated to be approximately $20\,\mu$m. The optimized configuration with cylindrical lens displays to a notable improvement in the signal-to-noise ratio, compared to the configuration without the cylindrical lens. As an example, we applied this new on-chip light-sheet configuration to the tracking and sizing of spherical gold nanoparticles with diameters of 80 nm and 50 nm in microfluidic channels.

The on-chip light sheet configuration presented here will be easily integrated in more elaborate microfluidic circuitry enabling control of mixing and diffusion for microscopic studies of nanoparticle self-assembly[48] and interaction with biomolecules[49]. It can be combined with in-channel microelectrodes for dielectrophoretically-assisted spectroscopic multicomponent analysis.[35] In its simplest form, integrated light sheet illumination of a microfluidic channel provides a flow cell for imaging cytometry[50] and for *in situ* optical microscopy and spectroscopy at the single-particle level with suppression of the out-of-focus background.

Author Contributions

Conceptualization: D.G., MHV.W. and M.L; project administration: D.G. and M.L.; modeling and simulation: T.T., D.G. and M.L.; experimental realization: all authors; data curation: T.T.; software: T.T., G.D. and M.L.; writing—original draft: T.T. and M.L.; writing—review and editing: all authors.

All authors have read and agreed to the published version of the manuscript.

Conflicts of interest

The authors declare no conflict of interest.

Acknowledgements

This research was funded by ANR under Project ANR-17-CE09-0009 SIPAIE (Aggregation Induced Emission at Single Particle level) and by project ANR-21-CE29-0020 MANBAMM (Multicomponent Analysis of Nano-Bio-Assemblies using Microfluidic Modulation).

Notes and references

1 C. Bigg, *Stud. Hist. Philos. Sci.*, 2008, **39**, 312–322.
2 R. Pecora, *Nat. Phys. Sci.*, 1971, **231**, 73–75.
3 D. Magde, E. Elson and W. W. Webb, *Phys. Rev. Lett.*, 1972, **29**, 705–708.
4 R. Cerbino and V. Trappe, *Phys. Rev. Lett.*, 2008, **100**, 1–4.
5 E. B. Brown, E. S. Wu, W. Zipfel and W. W. Webb, *Biophys. J.*, 1999, **77**, 2837–2849.
6 C. Y. Soo, Y. Song, Y. Zheng, E. C. Campbell, A. C. Riches, F. Gunn-Moore and S. J. Powis, *Immunology*, 2012, **136**, 192–197.
7 T. Wagner, H.-G. Lipinski and M. Wiemann, *J. Nanopart. Res.*, 2014, **16**, 2419.
8 H. Siedentopf and R. Zsigmondy, *Ann. Phys.*, 1902, **315**, 1–39.
9 T. Mappes, N. Jahr, A. Csaki, N. Vogler, J. Popp and W. Fritzsche, *Angew. Chem. Int. Ed. Engl.*, 2012, **51**, 11208–11212.
10 J. G. Ritter, R. Veith, A. Veenendaal, J. P. Siebrasse and U. Kubitscheck, *PLoS One*, 2010, **5**, 1–9.
11 R. Blue and D. Uttamchandani, *J. Biophotonics*, 2016, **9**, 13–25.
12 M. H. V. Werts, V. Raimbault, M. Loumaigne, L. Griscom, O. Français, J. R. G. Navarro, A. Débarre and B. Le Pioufle, *Proc. SPIE*, 2013, **8595**, 85950W.
13 S. Camou, H. Fujita and T. Fujii, *Lab Chip*, 2003, **3**, 40–45.
14 M. H. V. Werts, F. Allix, O. Français, C. Frochot, L. Griscom, B. Le Pioufle, M. Loumaigne and J. Midelet, *IEEE J. Sel. Top. Quant. Electron.*, 2014, **20**, 1–13.
15 E. J. Vargas-Ordaz, S. Gorelick, H. M. York, B. Liu, M. L. Halls, S. Arumugam, A. Neild, A. de Marco and V. J. Cadarso, *Lab Chip*, 2021, **21**, 2945–2954.
16 H. Jiang, T. Zhu, H. Zhang, J. Nie, Z. Guan, C. M. Ho, S. Liu and P. Fei, *Lab Chip*, 2017, **17**, 2193–2197.
17 C. Haiden, T. Wopelka, M. Jech, F. Keplinger and M. J. Vellekoop, *Langmuir*, 2014, **30**, 9607–9615.
18 P. Paiè, F. Bragheri, A. Bassi and R. Osellame, *Lab Chip*, 2016, **16**, 1556–1560.
19 H. Deschout, K. Raemdonck, S. Stremersch, P. Maoddi, G. Mernier, P. Renaud, S. Jiguet, A. Hendrix, M. Bracke, R. Van Den Broecke, M. Röding, M. Rudemo, J. Demeester, S. C. De Smedt, F. Strubbe, K. Neyts and K. Braeckmans, *Nanoscale*, 2014, **6**, 1741–1747.
20 A. H. Voie, D. H. Burns and F. A. Spelman, *J. Microsc.*, 1993, **170**, 229–236.
21 J. Huisken, J. Swoger, F. D. Bene, J. Wittbrodt and E. H. K. Stelzer, *Science*, 2004, **305**, 1007–1009.
22 I. Albert-Smet, A. Marcos-Vidal, J. J. Vaquero, M. Desco, A. Muñoz-Barrutia and J. Ripoll, *Front. Neuroanat.*, 2019, **13**, 1–15.
23 V. G. Colin, T. Travers, D. Gindre, R. Barillé and M. Loumaigne, *Int. J. Adv. Manuf. Technol.*, 2021, **116**, 537–544.

24 P. Vulto, N. Glade, L. Altomare, J. Bablet, L. D. Tin, G. Medoro, I. Chartier, N. Manaresi, M. Tartagni and R. Guerrieri, *Lab Chip*, 2005, **5**, 158.

25 K. Haubert, T. Drier and D. Beebe, *Lab Chip*, 2006, **6**, 1548–1549.

26 E. Hecht, *Optics*, Pearson, 2012.

27 F. Schneider, J. Draheim, R. Kamberger and U. Wallrabe, *Sens. Actuators, A*, 2009, **151**, 95–99.

28 K. H. Brenner and W. Singer, *Appl. Opt.*, 1993, **32**, 4984–4988.

29 L. M. Sanchez Brea, *diffractio: Python module for diffraction and interference optics*, `https://pypi.org/project/diffractio/`, 2019.

30 M. Berek, *Zeitschrift fur Physik*, 1927, **40**, 420–450.

31 H. Kirshner, D. Sage and M. Unser, *Proc. of the Twelfth Int. Conf. on Methods and Applications of Fluorescence Spectroscopy, Imaging and Probes*, 2011, 54.

32 H. Qian, M. P. Sheetz and E. L. Elson, *Biophys. J.*, 1991, **60**, 910–921.

33 J. T. Bullerjahn, S. Von Bülow and G. Hummer, *J. Chem. Phys.*, 2020, **153**, 024116.

34 A. J. Berglund, *Phys. Rev. E*, 2010, **82**, 1–8.

35 C. Midelet and M. H. V. Werts, *Part. Part. Syst. Charact.*, 2020, **37**, 2000187.

36 J. Midelet, A. H. El-Sagheer, T. Brown, A. G. Kanaras and M. H. V. Werts, *Part. Part. Syst. Charact.*, 2017, **34**, 1700095.

37 C. Bohren and D. Huffman, *Absorption and Scattering of Light by Small Particles*, Wiley, 2008.

38 J. Pawley, *Handbook of Biological Confocal Microscopy*, Springer US, 2010.

39 D. G. Beadle, *Nature*, 1940, **145**, 1018–1019.

40 D. Ershov, M.-S. Phan, J. W. Pylvänäinen, S. U. Rigaud, L. Le Blanc, A. Charles-Orszag, J. R. W. Conway, R. F. Laine, N. H. Roy, D. Bonazzi, G. Duménil, G. Jacquemet and J.-Y. Tinevez, *Nat. Methods*, 2022, **19**, 829–832.

41 C. L. Vestergaard, P. C. Blainey and H. Flyvbjerg, *Phys. Rev. E*, 2014, **89**, 022726.

42 S. S. Koyagura, H. Takehara and T. Ichiki, *J. Photopolym. Sci. Technol.*, 2020, **33**, 485–490.

43 C. Mack, *Fundamental Principles of Optical Lithography: The Science of Microfabrication*, Wiley, 2008.

44 J. G. Mehtala and A. Wei, *Langmuir*, 2014, **30**, 13737–13743.

45 C. Boutin, R. Jaffiol, J. Plain and P. Royer, *J. Fluoresc.*, 2008, **18**, 1115–1122.

46 X. Tian, M. R. Nejadnik, D. Baunsgaard, A. Henriksen, C. Rischel and W. Jiskoot, *Journal of Pharmaceutical Sciences*, 2016, **105**, 3366–3375.

47 M. A. Sahin, M. Shehzad and G. Destgeer, *Small*, 2023, 2307956.

48 M. Loumaigne, C. Midelet, T. Doussineau, P. Dugourd, R. Antoine, M. Stamboul, A. Débarre and M. H. V. Werts, *Nanoscale*, 2016, **8**, 6555–6570.

49 C. Chen, C. Midelet, S. Bhuckory, N. Hildebrandt and M. H. V. Werts, *J. Phys. Chem. C*, 2018, **122**, 17566–17574.

50 A. Kleiber, A. Ramoji, G. Mayer, U. Neugebauer, J. Popp and T. Henkel, *Lab Chip*, 2020, **20**, 1676–1686.